Modeling cell migration regulated by cell extracellular-matrix micromechanical coupling

Yu Zheng,[1,*] Hanqing Nan,[2,*] Yanping Liu,[3,*] Qihui Fan,[4,5,*] Xiaochen Wang,[4,5] Ruchuan Liu,[3] Liyu Liu,[3,†] Fangfu Ye,[4,5,‡] Bo Sun,[6,§] and Yang Jiao[2,1,¶]

[1]*Department of Physics, Arizona State University, Tempe, Arizona 85287, USA*
[2]*Materials Science and Engineering, Arizona State University, Tempe, Arizona 85287, USA*
[3]*College of Physics, Chongqing University, Chongqing 401331, China*
[4]*Beijing National Laboratory for Condensed Matte Physics and CAS Key Laboratory of Soft Matter Physics, Institute of Physics, Chinese Academy of Sciences, Beijing 100190, China*
[5]*School of Physical Sciences, University of Chinese Academy of Sciences, Beijing 100049, China*
[6]*Department of Physics, Oregon State University, Corvallis, Oregon 97331, USA*

(Received 25 May 2019; published 11 October 2019)

Cell migration in fibrous extracellular matrix (ECM) is crucial to many physiological and pathological processes such as tissue regeneration, immune response, and cancer progression. During migration, individual cells can generate active pulling forces via actomyosin contraction, which are transmitted to the ECM fibers through focal adhesion complexes, remodel the ECM, and eventually propagate to and can be sensed by other cells in the system. The microstructure and physical properties of the ECM can also significantly influence cell migration, e.g., via durotaxis and contact guidance. Here, we develop a computational model for two-dimensional cell migration regulated by cell-ECM micromechanical coupling. Our model explicitly takes into account a variety of cellular-level processes, including focal adhesion formation and disassembly, active traction force generation and cell locomotion due to actin filament contraction, transmission and propagation of tensile forces in the ECM, as well as the resulting ECM remodeling. We validate our model by accurately reproducing single-cell dynamics of MCF-10A breast cancer cells migrating on collagen gels and show that the durotaxis and contact guidance effects naturally arise as a consequence of the cell-ECM micromechanical interactions considered in the model. Moreover, our model predicts strongly correlated multicellular migration dynamics, which are resulted from the ECM-mediated mechanical coupling among the migrating cell and are subsequently verified in *in vitro* experiments using MCF-10A cells. Our computational model provides a robust tool to investigate emergent collective dynamics of multicellular systems in complex *in vivo* microenvironment and can be utilized to design *in vitro* microenvironments to guide collective behaviors and self-organization of cells.

DOI: 10.1103/PhysRevE.100.043303

I. INTRODUCTION

Cell migration in fibrous extracellular matrix (ECM) is a complex dynamic process involving a series of intracellular and extracellular activities, including the development of filopodia, formation of focal adhesion sites, locomotion due to actin filament contraction, and detachment of the rear end [1,2]. Collective cell migration in a complex microenvironment is crucial to many physiological and pathological processes including tissue regeneration, immune response, and cancer progression [3–6]. Besides the well-established chemotaxis [7], the microstructure and physical properties of the ECM can also significantly influence cell migration via durotaxis [8–10], haptotaxis [11], and contact guidance [12–14]. For example, in durotaxis, a cell can sense and respond to the rigidity gradient in the local microenvironment, which in turn guides its migration [10].

A migrating cell also generates active pulling forces [15–17], which are transmitted to the ECM fibers via focal adhesion complexes [18–20]. Such active forces remodel the local ECM, e.g., by reorienting the collagen fibers, forming fiber bundles, and increasing the local stiffness of ECM [21–27]. Recent studies have indicated that a delicate balance among the magnitude of the pulling forces, the cell-ECM adhesion strength, and the ECM rigidity is required to achieve an optimal mode of single cell migration [28]. In a multicellular system, the pulling forces generated by individual cells can give rise to a dynamically evolving force network (carried by the ECM fibers) in the system [29–37]. In other words, the active pulling forces generated by individual cells can propagate in the ECM and can be sensed by distant cells. This ECM-mediated mechanical coupling among the cells could further influence the migration of the individual cells, which in turn alters the ECM structure and properties, and thus the tensile force network. This feedback loop between the force network and cell migration could lead to a rich spectrum of collective migratory behaviors [36].

A variety of computational models have been developed to investigate the migration dynamics of both single cell and multicellular systems [38–40] as well as various sub-cellular

*These authors contributed equally to this work.
†lyliu@cqu.edu.cn
‡fye@iphy.ac.cn
§sunb@physics.oregonstate.edu
¶yang.jiao.2@asu.edu

processes involved in cell migration [41–46]. For example, a migrating cell can be modelled as an "active particle" whose dynamics is mainly determined by an active self-propelling force, a random drift and various effective particle-particle and/or particle-environment interactions [47,48]. A wide spectrum of collective dynamics have been observed and investigated in active-particle systems [48]. However, vertex-based models [49] and multistate cellular Potts models [50] are usually employed to investigate the collective dynamics of densely packed sheets of cells, including the spontaneous cell sorting driven by differential adhesion and the epithelial to mesenchymal transition (EMT). In addition, cellular automaton models which explicitly consider the migration of invasive tumor cells following least-resistance paths have been devised to study the emergence of invasive dendritic structures composed of highly malignant tumor cells emanating from the primary tumor mass [51–54].

Recently, the influences of the cell-ECM interactions and/or ECM-mediated indirect cell-cell interactions on individual and collective migration dynamics are started to be explicitly considered and incorporated in cell migration models [55,56]. For example, Goychuk *et al.* [57] introduced a cellular Potts model for cell migration that includes basic cell-ECM coupling. A computational model based on continuum mechanics has been developed that explicitly considers the micromechanical coupling of a migrating cell and the 2D substrate [58]. Durotaxis effects have been successfully reproduced from this model. Moreover, a novel model for investigating cell migration in a model 2D ECM network guided by external mechanical cues has been developed by considering coarse-grained cytoskeleton of a migrating cell as a part of the ECM network [59]. Very recently, the 2D vertex cell model is coupled to an elastic network of springs modeling the ECM, through dynamic focal adhesions attached to the network nodes, which has been employed to understand the effect of substrate stiffness on collective migration during wound healing and to measure traction forces during cell migration [60–62]. A recently developed migration model based on mechanical coupling of a model cell and lattice model of ECM network has successfully reproduced the durotaxis and contact guidance effects [63]. In addition, a variety of models have been developed for 3D cell migration in complex microenvironments [64–66].

Here, we develop a computational model for 2D migration of nonmetastatic breast cancer cells on top of a 3D collagen gel, which is mainly regulated by cell-ECM micromechanical coupling. Our model takes into account a variety of cellular-level processes including focal adhesion formation and disassembly, active traction force generation and cell locomotion due to actin filament contraction, transmission and propagation of tensile forces in the ECM. We employ a node-bond (i.e., graph) representation to model the complex 3D ECM network microstructure, which is reconstructed based on confocal imaging data. In addition, we use a nonlinear mechanical model for the ECM networks, which incorporates buckling of collagen fibers upon compression and strain-hardening upon stretching. We consider that the active forces generated by actin filament contraction are locally balanced at the focal adhesion site via the deformation of the ECM, which provides both mechanical support for cell migration and a medium for the propagation and transmission of the active cellular forces.

We validate our model by accurately reproducing single-cell dynamics of MCF-10A breast cancer cells migrating on collagen gels and show that the durotaxis and contact guidance effects naturally arise as a consequence of the cell-ECM micromechanical interactions considered in the model. Moreover, our model predicts strongly correlated multicellular migration dynamics, which are resulted from the ECM-mediated mechanical coupling among the migrating cells and are subsequently verified in *in vitro* experiments using MCF-10A cells. The current model can be readily generalized to model 3D cell migration in ECM and could eventually be employed to investigate collective migratory behaviors and emergent self-organizing multicellular patterns resulted from ECM-mediated mechanical signaling among the cells.

The rest of the paper is organized as follows: In Sec. II, we describe the microstructural and mechanical models of the 3D ECM (mainly collagen I) networks. In Sec. III, we introduce our cell migration model and discuss the associated assumptions and limitations. In Sec. IV, we validate our model by producing single-cell migration dynamics of MCF-10A breast cancer cells on isotropic collagen networks and investigate the cell migration dynamics on heterogeneous networks with stiffness gradient and aligned fibers. In Sec. V, we investigate collective multicellular dynamics resulting from ECM-mediated mechanical coupling among the migrating cells, and we validate our results via *in vitro* experiments. In Sec. VI, we provide concluding remarks.

II. MICROSTRUCTURE AND MECHANICAL MODELS OF 3D ECM NETWORK

A. Modeling ECM network via statistical descriptors and stochastic reconstruction

In this section, we briefly describe the microstructural and micromechanical models for the 3D ECM networks. The detailed descriptions of these models are provided in Refs. [67] and [35], respectively. The 3D ECM, mainly composed of type I collagen gel, is modeled as a discrete network with a "graph" (i.e., node-bond) representation in a cubic simulation domain with linear size L ($\sim$300 μm), which is composed of M_n nodes and M_b bonds, depending on the collagen concentration. The average coordination number Z, i.e., the average number of bonds connected to each node, is given by $Z = 2M_b/M_n$. We mainly use fixed boundary (FB) conditions (i.e., the nodes within a certain distance $\delta L \sim 5\,\mu$m from the boundaries of the simulation domain are fixed) in our simulations, but also confirm that using periodic boundary (PB) conditions does not affect the results for the large L values used in our simulations.

We employ a set of statistical descriptors for quantifying the network geometry and topology [67,68], which include the node density ρ (corresponding to the collagen concentration), the fiber (or bond) length distribution function P_f, the distribution of coordination number (i.e., the number of neighbors of a node) P_Z, and the average fiber orientation Ω. In particular, Ω is defined as the average cosine value associated with the acute angles of the fibers made with respect to a prescribed

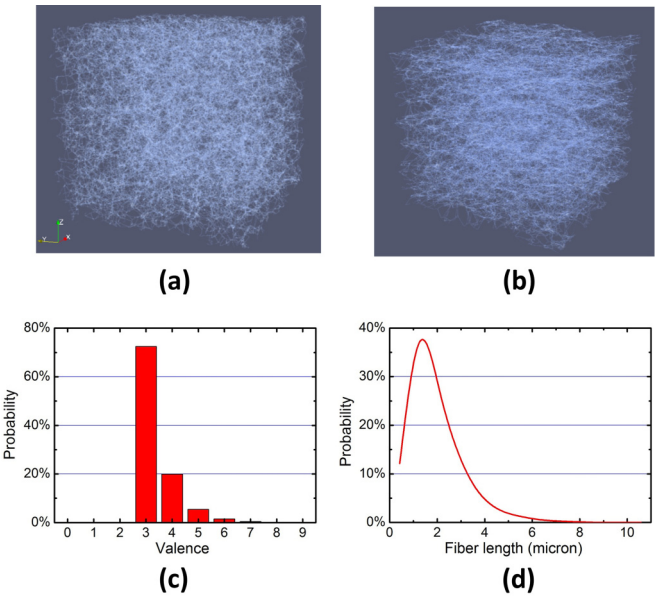

FIG. 1. Realizations of 3D ECM networks with randomly oriented fibers with $\Omega = 0.5$ (a) and horizontally aligned fibers with $\Omega = 0.88$ (b), generated using stochastic reconstruction techniques. For better visualization, only small subnetworks with a linear size of $50\,\mu$m are shown here. Panels (c) and (d), respectively, show the coordination distribution P_Z and fiber length distribution P_f for the networks, which are computed based on confocal images of a 2 mg/ml collagen gel. The statistical descriptors of the simulated networks almost perfectly match the corresponding target descriptors obtained from the experiments and thus, are visually indistinguishable from one another.

direction (typically along one of the three orthogonal axis of the simulation box). These statistical descriptors can be computed from the 3D ECM network extracted from the confocal images via skeletonization techniques [22]. Figures 1(c) and 1(d), respectively, show the coordination distribution P_Z and fiber length distribution P_f for homogeneous collagen networks with a collagen concentration of 2 mg/ml, which will be used in our subsequent investigations. The average fiber length is $1.96\,\mu$m and the average coordination number $Z = 3.4$ [35]. Since the fibers are randomly oriented in homogeneous networks, the average fiber orientation metric $\Omega \approx 0.5$. The node number density $\rho \approx 0.185/\mu\text{m}^3$.

For a given set of network statistics (e.g., P_Z^*, P_f^*, Ω^*, and ρ^*), we can generate realizations of the networks associated with the prescribed descriptors using stochastic reconstruction [67]. In particular, we start from a randomly generated initial network with the prescribed node number density ρ^*. From this initial network, the descriptors P_f, P_Z, and Ω are computed and compared to the corresponding prescribed descriptors. An energy functional E is defined as the sum of the squared differences between the computed and corresponding prescribed the descriptors [67], i.e.,

$$E = \sum_r |P_Z(r) - P_Z^*(r)|^2 + \sum_r |P_f(r) - P_f^*(r)|^2 + |\Omega - \Omega^*|^2. \quad (1)$$

Next, the initial network is perturbed by randomly displacing a node and/or removing/adding a bond to randomly selected pairs of nodes. A new energy for the new network is computed. If the new energy E_{new} is lower than the old energy E_{old}, the new network replaces the old one. Otherwise, the new network configuration replaces the old network with the probability $e^{(E_{\text{old}}-E_{\text{new}})/T}$, where T is a virtual temperature, which possesses a large initial value and is gradually decreased. The network is continuously evolved in this way (more precisely, via simulated annealing method [69] to allow energy-increasing network configurations during the initial stages) until $E \approx 0$, i.e., the computed descriptors match the prescribed ones within a prescribed small tolerance. The details of this technique is provided in Ref. [67].

We note that one can either use experimentally obtained network statistics as the target descriptors in the reconstruction or can construct a set of feasible hypothetical statistical descriptors in order to control the geometry and topology of the constructed random network. Figure 1(a) shows a reconstructed network based on the experimentally obtained statistics of the 2 mg/ml collagen gels, in which the fibers are randomly oriented. To investigate the effects of fiber alignment on cell migration dynamics, we also generate realizations of networks with horizontally aligned fibers [see Fig. 1(b)]. This is achieved by setting $\Omega^* = 1$ with respect to the x direction, and using the same P_Z^*, P_f^*, and ρ^* of the homogeneous network. We note that the optimized Ω of the reconstructed network is in fact a little smaller than unity ($\Omega \sim 0.88$), due to the additional topological and geometrical constraints specified by P_Z^* and P_f^*. Nevertheless, the fiber alignment is already very significant in the reconstructed networks.

B. Micromechanical model of ECM networks

The ECM (collagen) fibers are highly nonlinear, typically exhibiting buckling, strain-hardening and plastic behaviors [22,70–75], which can significantly affect the propagation of the active forces in the system. The nonlinearity of the ECM fibers also induces a nontrivial coupling with the cell contractility, i.e., for small contraction, the fibers may be in the linear elastic regime, while for large contraction, the fibers may be in the strain-hardening or plastic regime [35]. This in turns can affect the overall cell migration dynamics [28].

In this work, we will use a nonlinear micromechanical model for the ECM fiber, which is schematically illustrated in Fig. 2 [35,72]. In particular, upon stretching, a fiber first enters a linear elastic regime, which is followed by a strong strain-hardening regime once the elongation is larger than a prescribed threshold. Upon compression, we consider the fiber immediately buckles and thus, possesses a much smaller compression modulus. The elongation stiffness k of the fiber is thus given by

$$k = \begin{cases} \rho EA/\ell, & \lambda < 0, \\ EA/\ell, & 0 < \lambda < \lambda_s, \\ EA\exp[(\lambda - \lambda_s)/\lambda_0]/\ell, & \lambda > \lambda_s. \end{cases} \quad (2)$$

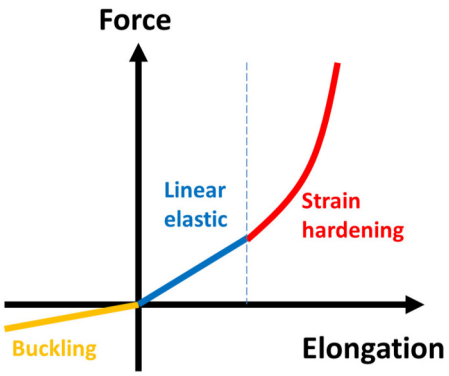

FIG. 2. Schematic illustration of the nonlinear elastic fiber model, including a linear elastic regime, which is followed by a strong strain-hardening regime upon compression and buckling upon compression.

where E and A are, respectively, the Young's modulus and cross-sectional area of the fiber bundle, and we use $EA = 8\times10^{-7}N$ [22]; $\lambda = \delta\ell/\ell$ is elongation strain, ℓ is the original fiber length, and $\lambda_s = 0.02$ and $\lambda_0 = 0.05$ are parameters for the strain-hardening model [72]; $\rho = 0.1$ describes the effects of buckling [35]. In addition, we consider the fiber segments as well as the cross links (nodes) can resist bending and employ a first-order bending approximation [73], for which the bending energy E_b is a function of transverse displacement u of the two nodes of a fiber, i.e., $E_b = \alpha EIu^2/\ell_0$, where the bending modulus $EI = 5\times10^{-22}\,\mathrm{Nm}^2$ [22], I is the second moment of area, ℓ_0 is the original length of the fiber segment, and $\alpha = 1.8$. We also note that the effects of interstitial fluid, which quickly dissipates the kinetic energy generated due to cell contraction, are not explicitly considered.

Plasticity of the fibers is modeled as a time-dependent elongation of the fiber with a constant flow rate γ, i.e., $\delta l_P = \gamma t$, once the stretching force on the fiber is larger than a prescribed threshold f_P. The flow rate can be calibrated based on experimental data available in literature [26]. We note that this elongation due to plasticity effectively reduces the stiffness of the fiber, i.e., $k = EA/(\ell + \delta\ell_P)$. In addition, we can easily construct a stiffness gradient in the ECM network, by introducing a position-dependent scaling factor, i.e., $E(x) = EC_0(x)$, where $C_0(x) = (1 + x/L)$. It is clear that other forms of $C_0(x)$ than the simple linear scaling could be employed to model more complex stiffness gradient. We note that a more realistic implementation of the stiffness gradient is to vary the mesh size of the network. This can be achieved using the stochastic network reconstruction technique, in which node density is systematically varied from low to high along the direction of varying stiffness. Nonetheless, we expect the artificial approach used here would not significantly change the physics involved in cell-ECM interaction in the context of local durotaxis: In both cases (artificially varying stiffness/varying mesh size), a cell "feels" the local stiffness via the displacement at focal adhesion once active pulling is applied. Therefore, in the subsequent studies, we will use the simple constant gradient to investigate the durotaxis effects.

Once the cell contractions are applied (as described in Sec. III), an iteration procedure [35] will be employed to find the force-balanced state of the network and obtain the forces on the fibers. The numerical procedure can be easily parallelized using OpenMP for large networks.

III. MODELING CELL MIGRATION REGULATED BY CELL-ECM MICROMECHANICAL COUPLING

In this section, we present in detail the cell migration model, which is coupled with the ECM network model. We note that the current model is targeted for motile but non-metastatic cancer cells, such as the MCF-10A breast cancer cells, which move on top of a thick layer of collagen gel. In this case, the migrating cells are coupled with the ECM via their micromechanical interactions, without any ECM degradation (such as that through cell-secreted MMP in the case of metastatic MDA-MB-231 breast cancer cells). Therefore, we do not consider ECM degradation in the current model and the associated cell invasion into the ECM layer. However, including such events is straightforward, as we will discuss briefly in Sec. VI.

As illustrated in Fig. 3, our cell model consists of an elastic sphere representing the exclusion volume associated with cytoplasm and a set of actin filaments that can extend beyond the cytoplasm sphere to develop protrusions, which are attached to the ECM network via focal adhesion at the network nodes. As a starting point, we will not explicitly consider microtubule, and intermediate filaments, and only focus on the contractility of the actin filaments. The plasma membrane is then modeled as the minimal hull enclosing the end points of the filaments [see Fig. 3(a)]. In the beginning of the simulation, a cell (i.e., a cytoplasm sphere and the associated cytoskeleton filaments) is introduced in the collagen network, and a random persistent direction $\mathbf{n}_0$ is selected. The migration process is decomposed into cycles of successive events, including (i) development of protrusion (due to active actin filaments polymerization) and formation of new adhesion sites, (ii) contraction of actin filaments and the resulting locomotion of the cell, and (iii) breaking of old adhesion sites. These events are modeled and simulated as described below:

(i) Protrusions are generated by the elongation (polymerization) of the actin filaments, which can be attached to the ECM fibers via focal adhesion complexes. This process is modeled by adding new filaments connecting the center of mass of the cell (i.e., the center of the cytoplasm sphere) to a node of the ECM network within $\delta R_s \sim 5\,\mu$m (effective protrusion length) from the cell surface [see Figs. 3(a) and 3(b)], selected with the probability p_a given by

$$p_a \sim c_1(\mathbf{n}_0 \cdot \mathbf{d}) + c_2\sigma_f, \tag{3}$$

where $\mathbf{n}_0$ is the persistent direction of the cell, $\mathbf{d}$ is vector connecting the cell center and the network node, σ_f is the largest stress on the fibers connected to the node, $c_1 = 1/|\mathbf{d}|$ (where $|\mathbf{d}|$ is the length of the vector $\mathbf{d}$)and $c_2 = 1/\sigma_0$ (where σ_0 is the average stress over all fibers in the network) are proportionality constants. The relative probability p_a^i for possible new filament i is first computed according to Eq. (3) for all possible new filaments, and then is normalized by the factor $\sum_i p_a^i$. This model implies that the actin filament polymerization is more likely to occur in the polarized region

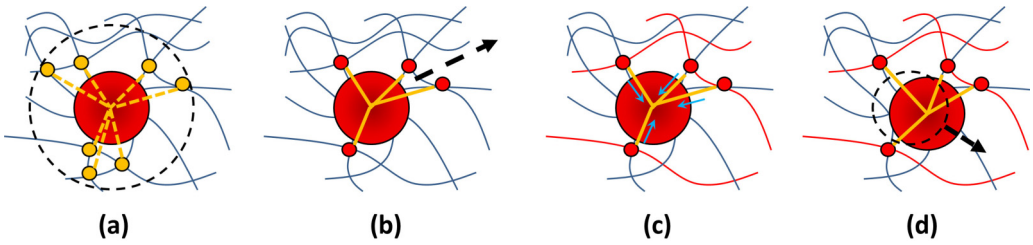

FIG. 3. Schematic illustration of the computational model for a migrating cell. (a) Protrusions (yellow dashed lines) generated by polymerization of actin filaments can lead to focal adhesion formation (yellow dots) in a region within δR_s (effective protrusion length) from the cell surface (red sphere), which is enclosed by the dashed circle. (b) New focal adhesion (red dots) formation is modeled by adding new filaments (yellow solid lines) connecting the center of mass of the cell (i.e., the center of the cytoplasm sphere) to a randomly selected node of the ECM network within δR_s from the cell surface, with a probability depending on the persistent direction of the cell (dashed arrow) and the local stress state of the fibers. (c) Active contraction of actin filaments generates active forces in the ECM network and leads to deformation of ECM. (d) Locomotion of the cell due to actin filament contraction.

of the cell [15]; and that it is more likely to form an adhesion site on highly stressed fibers [18,20]. Each adhesion site has a finite life span T_a and breaks once T_a is reached.

(ii) The contraction of an actin filament connecting the cytoplasm sphere and a network node can generate a traction force $\mathbf{f}_t$ ($\sim$1 nN) along the filament direction [76–79] and a shrinkage of the filament length δl ($\sim$10% of the original length); see Fig. 3(c). This active force is transmitted to the ECM network through the "focal adhesion" node. Force boundary condition is imposed to this node (and other nodes connected to contracting filaments) and the deformed force-balanced network configuration is obtained as described in Sec. II B. The length d' of the filament connecting the center cell and the displaced node is then computed. We then consider the contraction of this filament generates a displacement component for the cell enter, i.e.,

$$\delta\mathbf{x} = \max\{\delta l - (d - d'), 0\} \cdot \mathbf{d}_0', \tag{4}$$

where δl is the intrinsic contraction of the filament, d and d' are, respectively, the distance between the cell center and the adhesion node before and after ECM deformation due to filament contraction, and $\mathbf{d}_0'$ is the unitary direction vector along the filament direction after ECM deformation.

(iii) Once the displacement components associated with all filaments are computed, the center of mass position of the cell is updated as follows [see Fig. 3(d)]:

$$\mathbf{x}_{t+1} = \mathbf{x}_t + \sum_i \delta\mathbf{x}_i, \tag{5}$$

where the sum is taken for all filaments, and $\delta\mathbf{x}_i$ is the displacement component associated with the ith filament. The persistent direction $\mathbf{n}_0$ is updated as the direction of the cell displacement (i.e., $\sum_i \delta\mathbf{x}_i$). We note that Eqs. (4) and (5) imply that cell locomotion is due to actin filament contraction and depends on the stiffness of the local ECM.

(iv) All of the current adhesion sites (nodes) are checked and those reach their life span T_a will break, leading to the detachment of the cell from the ECM network.

In the simulation, time is discretized such that a migration cycle is completed during the elapsing of one time step $dt \sim 1$ min. In other words, one time step includes all cellular processes (e.g., protrusion, focal adhesion formation, actin contraction, locomotion and bond breaking, etc.) for a complete migration cycle. The actual time associated with a particular cellular process is not resolved within a migration cycle. The life span of a focal adhesion T_a is chosen such that the adhesion bond is broken after two complete migration cycles, i.e., $T_a = 2dt$. This is calibrated based on the experimental data (see Sec. IV for details), and allows us to successfully reproduce the experimentally observed migration dynamic with the correct time scale. Choosing a larger T_a will effectively slow down the migration in the simulations, but will not qualitatively change the migration behavior. The life span can also be randomly chosen from a distribution. However, we expect that this would not affect the overall simulated migration dynamics on this level of time resolution. Once an entire migration cycle is completed, the position of the cytoplasm sphere (and thus, the center of mass of the cell) is updated and the cell starts the next migration cycle, by repeating the steps (i) to (iv).

We also note that the cell-cell contact adhesion is not explicitly considered in this model, since our focus here is motile mesenchymal breast cancer cells with relatively weak cell-cell adhesion. In addition, we employ a minimal model for the contact inhibition effect for multicellular systems. In particular, we consider that if a pair of cells with radius R_s ($=10\,\mu$m) overlap, they feel a mutual repulsive force proportional to the linear overlap distance, i.e., $F_r = \kappa\delta R$, where κ is an effective elastic constant depending on the modulus of the cell, $\delta R = 2R_s - d_s$ is the overlap distance, and d_s is the cell center separation distance. In the current model, since the cells are constrained to only move on the surface of the ECM, we do not explicitly consider the mechanical interaction between the cytoplasm exclusion sphere and the ECM fibers.

The key model parameters discussed above are summarized in Table I. The key steps for implementing the cell migration model are summarized below:

(i) *Initialization*: ECM network is initialized; the cell (cytoplasm sphere) is introduced at a prescribed position on the top surface of the ECM network; an initial persistent direction is assigned.

(ii) *Focal adhesion formation*: Check all nodes of the network within a distance of δR_s from the cell surface; connect the nodes to the cell center with probability p_a [cf. Eq. (3)] by a (virtual) filament.

TABLE I. Summary of key parameters for the cell migration model.

Symbol	Definition	Numerical Value
R_s	Cell radius	10 μm
δR_s	Effective protrusion length from the cell surface	5 μm
$\mathbf{n}_0$	Persistent direction of cell migration	—
$\mathbf{d}_0$	Unitary vector connecting cell center to a focal adhesion node	—
d	Distance from the cell center to a focal adhesion node	—
$\mathbf{d}_0'$	Unitary vector connecting cell center to a focal adhesion node after the ECM deformation	—
d'	Distance from the cell center to a focal adhesion node after the ECM deformation	—
p_a	Probability of focal adhesion formation	cf. Eq. (3)
$\mathbf{f}_t$	Active tensile force generated via actin filament contraction	1 nN
δl	Shrinkage of effective actin filament length	10% of the original length
T_a	Lifespan of focal adhesion bond	two migration cycles
κ	Effective stiffness of a cell	1 nN/μm
dt	Discrete time step	1 min

(iii) *Actin filament contraction*: For each network node connecting to the cell center by a filament, impose the force boundary condition by applying a tensile force of 1 nN at the node pointing to the cell center; solve the forces and the deformation of all fibers of the network using the micromechanical model described in Sec. II B.

(iv) *Cell locomotion*: For each filament i, compute its contribution to the cell center displacement $\delta\mathbf{x}_i$ according to Eq. (4); then compute the displacement of the cell center by superposing the displacement contributions from all filaments [cf. Eq. (5)]; update the center position according to Eq. (5); update the length of all filaments.

(v) *Breaking adhesion bond*: Check the life of all existing filaments and delete those that have reached their life span T_a.

(vi) Repeat steps (ii)–(v) for a prescribed number of cell cycles.

In the subsequent sections, we will validate our model using single-cell migration experiments and employ the model to predict multicell migration dynamics.

IV. SINGLE-CELL MIGRATION DYNAMICS

In this section, we employ our model to investigate single cell migration dynamics and its regulation by the microstructure and mechanical properties of the microenvironment (i.e., the ECM network). We mainly focus on nonmetastatic MCF-10A breast cancer cells in our simulations [80]. These cells have relatively high motility but are not able to invade since the pores in the ECM are too small and the cells cannot produce MMP to degrade the ECM (in contrast to the metastatic MB-MDA-231 cells). For the 2 mg/ml collagen used in the study, the average fiber length is about 2 μm, and the average pore size is about 5 μm, which is much smaller the linear size of the cell ($\sim$20 μm). In addition, there is no "driving force" such as a nutrient/glucose gradient for the cells to invade. Although not being able to invade, the strong motility of the MCF-10A cells induces strong cell-ECM mechanical coupling and can generate strong contractile forces during migration [80]. Using a thick layer of collagen gel is crucial to ensuring the propagation of the contractile forces through the ECM, which in turn induces correlated cell dynamics. Therefore, this system provides an ideal platform for testing our model. In the following discussions, we will directly use the experimental results to validate our model predictions. The experimental details are provided in Ref. [80].

A. Migration dynamics of MCF-10A cells on isotropic collagen gel

We first employ our model to study the migration dynamics of individual MCF-10A breast cancer cells on top of a thick layer of isotropic collagen gel with randomly oriented fibers. It is well established that in this case, the overall cell dynamics can be captured by the active-particle model [48], i.e.,

$$\gamma d\mathbf{r}/dt = F\hat{\mathbf{e}} + \xi, \tag{6}$$

where $\mathbf{r}$ is the particle center of mass, γ is an effective friction coefficient, F is an effective constant self-propelling force, $\hat{\mathbf{e}}$ is the persistent direction which is subject to a random rotational diffusion and ξ is a white-noise random vector [48]. The associated theoretical mean-squared displacement (MSD) σ^2 is given by [48]

$$\sigma^2(t) = [4D + 2v^2\tau_R]t + 2v^2\tau_R^2[e^{-t/\tau_R} - 1], \tag{7}$$

where D is the diffusivity of the particle, v is the persistent velocity and τ_R is the relaxation time for rotation diffusion of the persistent direction. It can be seen from Eq. (7) that for small t, the particle exhibits ballistic dynamics with $\sigma^2 \propto t^2$. At large t, the system is diffusive, with $\sigma^2 \propto \bar{D}t$, where $\bar{D} = 4D + 2v^2\tau_R$ is the effective diffusivity.

Figure 4 shows the 3D visualization of a single MCF-10A cell migrating on an isotropic collagen gel with randomly oriented fibers (see the left panel). The 3D collagen network model is obtained via stochastic reconstruction based on the structural statistics extracted from confocal images, as described in Sec. II A. The contraction of the actin filaments generates active tensile forces, which are transmitted to the collagen fibers and propagate in the ECM network. The fibers carrying large tensile forces are highlighted in red color. The right panel of the figure shows a confocal microscopy image of a migrating MCF-10A cell (bright blue) on an isotropic collagen gel. It can be seen that the collagen fibers in the vicinity of the cell surface tend to orient perpendicularly to

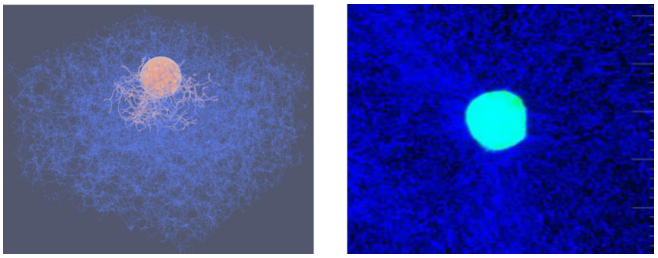

FIG. 4. Left panel: 3D visualization of a single MCF-10A cell migrating on isotropic collagen gel with randomly oriented fibers. The contraction of the actin filaments generates active tensile forces, which are transmitted to the collagen fibers (shown in red or dark gray in print version). Right panel: Confocal microscopy image of a migrating MCF-10A cell (bright blue) on collagen gel. The collagen fibers are shown in dark blue (or dark gray in print version). The linear size of the system is $\sim 100\,\mu$m.

the cell surface, implying that the cell generates traction forces and pulls the fibers, consistent with the simulation results.

Figure 5 shows the mean-squared displacement (MSD) of a single MCF-10A cell migrating on isotropic collagen gel with randomly oriented fibers, respectively, obtained from computer simulation (left panel) and *in vitro* experiment (right panel). The reported results are, respectively, ensemble averages of 15 independent experiments and 20 independent simulations. The regions enclosed by the dashed lines represent the range of standard deviations. The details of the experiments are provided in Ref. [80]. Here, we only present the experimental results relevant to our model. The initial ballistic dynamics (i.e., $\sigma^2 \propto t^2$) can be clearly seen, which is followed by the diffusive dynamics (i.e., $\sigma^2 \propto \bar{D}t$). The effective diffusivity of the cell obtained from the simulations and experiments are, respectively, $\bar{D} \approx 94\,\mu\text{m}^2/\text{min}$ and $\bar{D} \approx 103\,\mu\text{m}^2/\text{min}$, which agree well with one another.

The insets of Fig. 5 show the trajectories associated with an ensemble of migrating cells, respectively, obtained from the simulations and experiments. It can be clearly seen that the cell migration is isotropic, as expected for a cell in a homogeneous microenvironment without any externally applied cues.

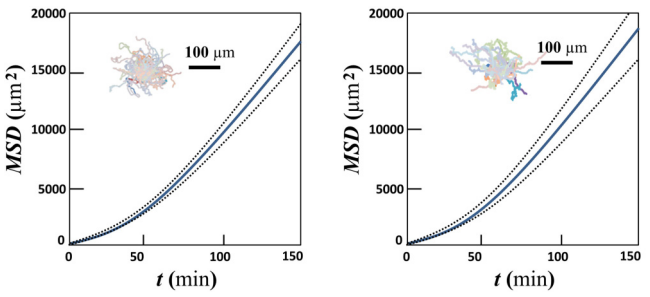

FIG. 5. Comparison of the mean-squared displacement (MSD) of a single MCF-10A cell migrating on isotropic collagen gel with randomly oriented fibers, respectively, obtained from computer simulation (left panel) and *in vitro* experiment (right panel). The reported results are, respectively, ensemble averages of 15 independent experiments and 20 independent simulations. The regions enclosed by the dashed lines represent the range of standard deviations. The insets show the trajectories of the cells.

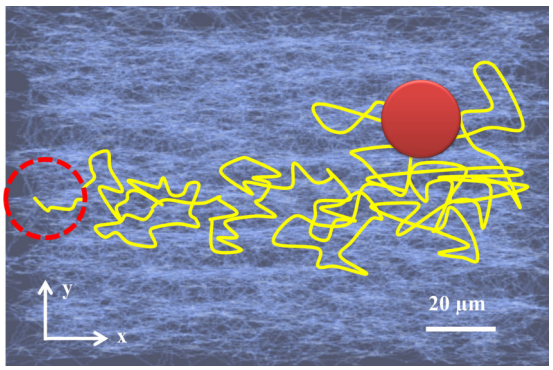

FIG. 6. A typical trajectory of MCF-10A cell migrating on 3D collagen gel with horizontally aligned fibers obtained from simulations.

We note that some trajectories from the experiments appear to be more persistent than those in the simulations. We believe the major reason for the apparent stronger persistence is that the experimental system exhibits larger fluctuations (as can be seen by the larger regions enclosed by the dashed lines representing the standard deviations). The more persistent trajectories are more apparent in the plot, and there are also less persistent trajectories that are masked in the center region of the plot. Nonetheless, the average dynamics as quantified by the MSD is consistent with the simulation results. These results clearly indicate the validity of our model.

B. Migration dynamics of MCF-10A cells on collagen gel with aligned fibers

With our model validated by experiments, we now employ it to study cell migration in complex microenvironment, such as collagen gels with aligned fibers, which are difficult to fabricate experimentally. The 3D virtual ECM networks are stochastically constructed by maximizing the fiber orientation metric Ω along the x direction (see Sec. II A for details). This leads to model networks with fibers mainly aligned along the x direction (see Fig. 6).

Figure 6 shows a typical trajectory of a MCF-10A cell migrating on a 3D collagen gel with horizontally aligned fibers obtained from simulations. It can be clearly seen that the cell tends to migrate along the direction consistent with the fiber alignment direction (e.g., in this case, x direction). This can also been seen quantitatively seen from the MSD analysis. Figure 7 shows the MSD of the migrating cell, respectively, along the x direction (left panel) and y direction (right panel). Anisotropy in the migration can be clearly observed, i.e., the cell moves much faster long the fiber alignment direction than the perpendicular direction. The effective diffusivity along the fiber alignment direction and the perpendicular direction is, respectively, $\bar{D}_\parallel \approx 168\,\mu\text{m}^2/\text{min}$ and $\bar{D}_\perp \approx 104\,\mu\text{m}^2/\text{min}$.

We note that the phenomenon that cells tend to migrate along the fiber alignment direction is well known and termed as "contact guidance" [12,13]. In particular, the symmetry is broken along the fiber alignment direction, and the cells can move both forward and backward (i.e., bidirectional), leading to stronger mixed persistent-diffusive migration behavior along this direction than the perpendicular direction.

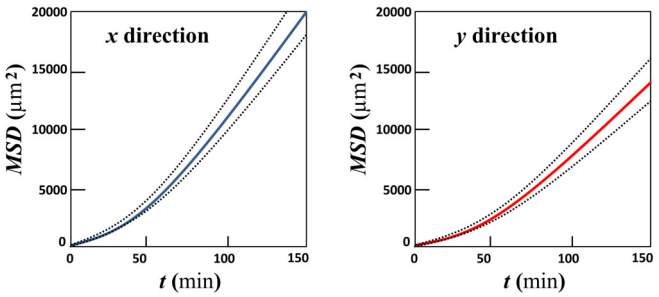

FIG. 7. Mean-squared displacement (MSD) of MCF-10A cell migrating on 3D collagen gel with horizontally aligned fibers (along the x direction), respectively, along the x direction (left panel) and y direction (right panel). Anisotropy in migration can be clearly observed, i.e., the cell tends to move along the direction of fiber aligned, a phenomenon known as contact guidance. The reported results are ensemble averages of 20 independent simulations. The regions enclosed by the dashed lines represent the range of standard deviations.

However, we are not able to separately characterize the diffusive and persistent behaviors in the migration dynamics at this stage. In our simulations, as the migrating cell pulls the ECM fibers, the large tensile forces are mainly carried by certain chains of aligned fibers, which are typically referred to as the "force chains" [35,67]. The high-stress fibers along the force chains are effectively stiffer (e.g., due to strain hardening) and thus, can support large-magnitude locomotion steps along the chain directions, and in this case, the fiber alignment direction. The simulated migration dynamics are consistent with those reported in Ref. [63].

C. Migration dynamics of MCF-10A cells on collagen gel with a stiffness gradient

We now employ our model to study cell migration dynamics on collagen gels with a stiffness gradient. As described in Sec. II A, the structural model of the 3D ECM is constructed based on the experimentally obtained statistics of a 2 mg/ml collagen gel with randomly oriented fibers. Once the 3D structural model is obtained, a linear stiffness distribution along x direction with a constant gradient is built. This is achieved by rescaling the Young's modulus of the fiber according to $E(x) = E(1 + x/L)$, where x is the x coordinate of the center of the fibers.

Figure 8 shows a typical trajectory of a MCF-10A cell migrating on a 3D collagen gel with a stiffness gradient along the x direction. Similar to the case of contact guidance, it can be clearly seen that the cell tends to migrate along the direction against the stiffness gradient, i.e., the positive x direction. This can also been seen quantitatively seen from the MSD analysis. Figure 9 shows the MSD of the migrating cell, respectively, along the x direction (left panel) and y direction (right panel). Anisotropy in the migration can be clearly observed, i.e., the cell moves much faster long the stiffness gradient direction than the perpendicular direction. The effective diffusivity along the stiffness gradient direction and the perpendicular direction is, respectively, $\bar{D}_{\parallel} \approx 146\,\mu\text{m}^2/\text{min}$ and $\bar{D}_{\perp} \approx 117\,\mu\text{m}^2/\text{min}$.

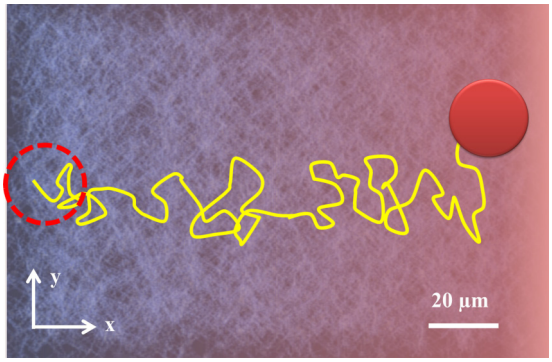

FIG. 8. A typical trajectory of MCF-10A cell migrating on 3D collagen gel with a stiffness gradient along the x direction obtained from simulations.

The phenomenon that cells migrate against the stiffness gradient of the ECM is well known and termed as "durotaxis" [8–10]. In our simulations, as the migrating cell pulls the ECM fibers, the stiffer fibers will possess smaller deformation, which in turn can support larger locomotion components towards these fibers [cf. Eq. (4)]. The accumulated effect of many local migration steps is the overall biased migration up the stiffness gradient as observed in the experiments.

We note that an important distinction between the migration anisotropy in this case and the contact guidance case is that here the cell migration is unidirectional, i.e., up the stiffness gradient; while in the contact guidance case, the migration is bidirectional, i.e., along the fiber alignment direction but the cells can move in both ways. Therefore, the migration dynamics for the durotaxis case is more ballistic as can be seen from the MSD data in Fig. 9. In particular, the quadratic part in the MSD remains significant for a longer time compared to the contact guidance case (see Fig. 7), but eventually the dynamics becomes diffusive. The simulated migration dynamics are consistent with those reported in Ref. [63].

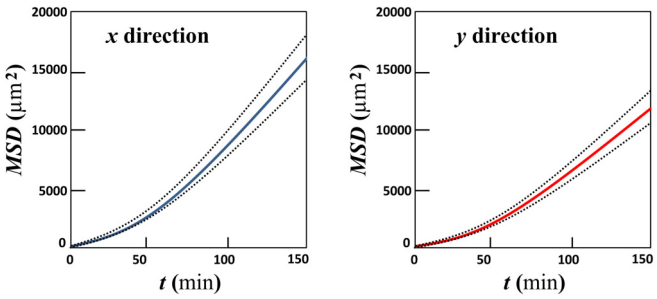

FIG. 9. Mean-squared displacement (MSD) of MCF-10A cell migrating on 3D collagen gel with a stiffness gradient (along the x direction), respectively, along the x direction (left panel) and y direction (right panel). Anisotropy in migration can be clearly observed, i.e., the cell tends to move up against the stiffness gradient, a phenomenon known as durotaxis. The reported results are ensemble averages of 20 independent simulations. The regions enclosed by the dashed lines represent the range of standard deviations.

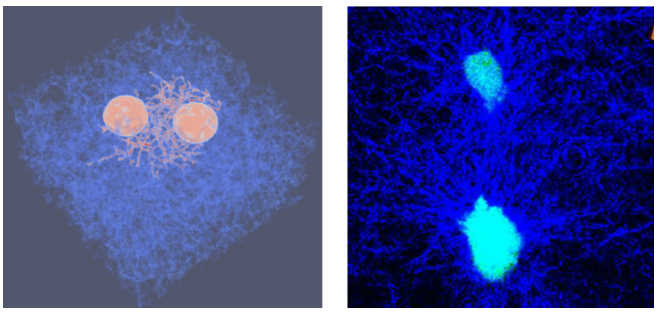

FIG. 10. Left panel: 3D visualization of two closely spaced MCF-10A cells migrating on an isotropic collagen gel with randomly oriented fibers. The collagen fibers carrying large tensile forces generated by actin filament contraction are highlighted in red. Right panel: Confocal microscopy image of a pair of migrating MCF-10A cells (bright blue) on collagen gel. The collagen fibers are shown in dark blue (or dark gray in print version).

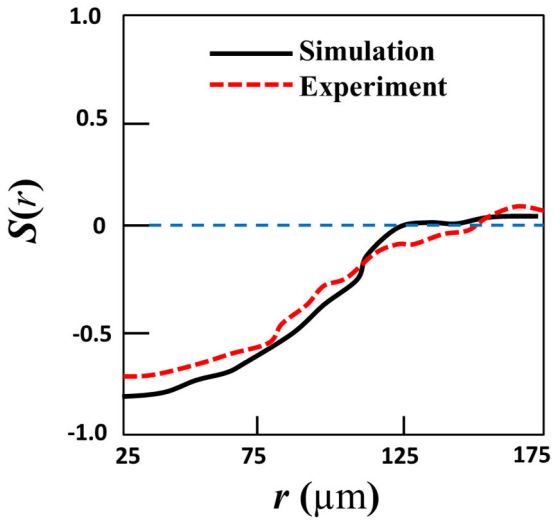

FIG. 11. Comparison of the velocity correlation function $S(r)$ (see the text for definition) of MCF-10A cells migrating on isotropic collagen gels with randomly oriented fibers, respectively, obtained from computer simulation (solid curve) and *in vitro* experiment (dashed curve).

V. STRONGLY CORRELATED MULTICELLULAR DYNAMICS

In Sec. IV, we show that our computational model can capture the salient features of single-cell migration dynamics in both homogeneous and complex microenvironment. In this section, we employ the model to investigate multicellular migration dynamics. As mentioned in Sec. III, we do not explicitly model cell-cell adhesion here (due to very low cell density considered here $\sim 0.0002\,\mu\text{m}^{-2}$) and use a minimal model for cell-cell repulsion due to contact inhibition (see Sec. III for details). In addition, in this study, we focus on relatively small system, containing ~ 20 cells.

Figure 10(a) shows 3D visualization of a small portion (with a linear size $\sim 50\,\mu$m) of the simulation box which contains two closely spaced MCF-10A cells migrating on isotropic collagen gel with randomly oriented fibers. The active tensile forces generated by the cells (due to actin filament contraction) are transmitted to the collagen fibers. The collagen fibers carrying large tensile forces (i.e., those that are larger than 10% of the maximal pulling force among all fibers) are highlighted in red. Figure 10(b) shows the confocal microscopy image of a pair of migrating MCF-10A cells (bright blue) on collagen gel. It can be clearly seen that the collagen fibers (dark blue) between the two cells form a mesoscopic scale structure, which is clearly distinguished from original homogeneous ECM network and is consistent with the mesoscale structure carrying the majority of tensile forces in between two contractile cells in our simulations.

We also quantify the average orientation of the fibers between the two cells using the orientation metric Ω^*, which is computed as the average cosine of the acute angles made by the fibers in this region with respect to the line connecting the cell centers. The orientation metric computed from the simulation and experimental data are, respectively, $\Omega^* = 0.794$ and 0.823, which is consistent with the observation based on the images. One possible reason for the observed stronger alignment of ECM fibers in the experimental system is that the ECM might also be chemically remodeled (e.g., forming fiber bundles and thus more visible under confocal microscopy) besides the mechanical remodeling as considered in the simulations.

To quantify the correlations in the collective migration dynamics of multiple MCF-10A cells, we employ the velocity correlation function $S(r)$, i.e.,

$$S(r) = \langle \mathbf{v}_i(\mathbf{x}) \cdot \mathbf{v}_j(\mathbf{x}+\mathbf{r}) \rangle / (|\mathbf{v}_i(\mathbf{x})||\mathbf{v}_j(\mathbf{x}+\mathbf{r})|), \qquad (8)$$

where $r = |\mathbf{r}|$, i, j denote a pair of cells connected by the remodeled mesoscale ECM structures and $\langle , \rangle$ denotes ensemble average over all different cell pairs. We note that in computing $S(r)$, we only consider a subsets of cell pairs, i.e., those between which the mesoscale fiber structures are formed. This allows us to clearly obtain the effects of such mesostructure on the collective dynamics of the cells, if any. Due to the mutual exclusion effects among the cells, $S(r) = 0$ for $r < D^*$ and D^* is roughly the diameter of a cell. In addition, two cells separated by very large distances are not correlated, i.e., $S(r) \approx 0$ for large r values. A positive $S(r)$ indicates that the cells tend to move in the same direction, implying a net "flow" of cells in the system. However, a negative $S(r)$ indicates that the cells move towards or away from one another. In the former case (i.e., cells moving towards one another), this implies the formation of aggregation or clusters at high cell densities.

We also note that although the radius of the idealized spherical cell in our modal is exactly 10 μm, consistent with the effective size of actual cells in the experiments (defined through equivalent area), the cell-center separation distance when two cells in contact in the experiments can significantly fluctuate (e.g., typically between 5 and 15 μm) due to the deformation of cell shapes. This can lead to unreliable statistics for the correlation function for small distances in the experimental case. Therefore, we have chosen a larger starting distance, i.e., $D^* = 25\,\mu$m (instead of 20 μm) for the correlation function calculation.

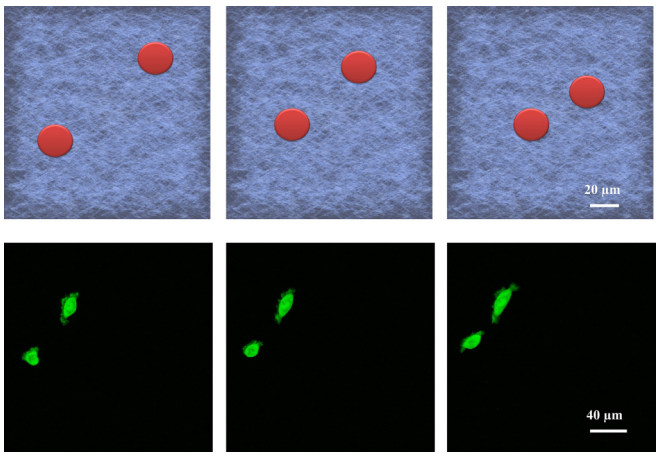

FIG. 12. Successive snapshots over 30 min showing the positions of two nearby cells obtained from simulations (upper panels) and experiments (lower panels). These results indicate the two cells move towards one another, as indicated by the short-range negative values of the corresponding velocity correlation functions shown in Fig. 11.

Figure 11 shows the velocity correlation function $S(r)$ of MCF-10A cells migrating on isotropic collagen gels with randomly oriented fibers, respectively, obtained from computer simulations (solid curve) and *in vitro* experiments (dashed curve). It can be seen that the simulation results agree very well with the experimental data. Interestingly, the $S(r)$ functions (beyond the trivial exclusion region) start from a very negative value (close to the minimal value -1) around $D^* \approx 25\,\mu$m, slowly increase to zero and then fluctuate around zero. Together with the visualizations of the simulation results (see Fig. 12), this indicates the cells tend to move towards one another, facilitated by the mesoscopic structures of the remodeled ECM, which is also confirmed by the time-lapse confocal data [80].

Our results indicate that strongly correlated cell migration dynamics is correlated with the mesoscale ECM structures due to cell remodeling. One possible reason is that the mesostructures are composed of many force chains (or a "force network"), which are in turn composed of fibers carrying large tensile forces. Therefore, the fibers in the mesostructures (at least in our simulations) are stiffer than the remaining stress-free fibers, which indicates that the mesostructures themselves are stiffer than the surrounding ECM. These stiffer mesostructures can then facilitate correlated cell migration via durotaxis, and also facilitate indirect mechanical coupling between the migrating cells.

VI. CONCLUSIONS AND DISCUSSION

In this paper, we develop a computational model for cell migration in complex microenvironment, which explicitly takes into account a variety of cellular-level processes including focal adhesion formation and disassembly, active traction force generation and cell locomotion due to actin filament contraction, transmission and propagation of tensile forces in the ECM. We employ statistical descriptors obtainable from confocal microscopy to quantify and control the 3D ECM network microstructure and use a nonlinear mechanical model for the ECM networks, which incorporates buckling of collagen fibers upon compression and strain-hardening upon stretching. We validate our model by accurately reproducing single-cell dynamics of MCF-10A breast cancer cells migrating on collagen gels and show that the durotaxis and contact guidance effects naturally arise as a consequence of the cell-ECM micromechanical interactions considered in the model. Moreover, our model predicts strongly correlated multicellular migration dynamics, which are resulted from the ECM-mediated mechanical coupling among the migrating cells and are subsequently verified in *in vitro* experiments using MCF-10A cells.

Although focusing on the nonmetastatic MCF-10A breast cancer cells migrating on top of thick layers of collagen gels, our model can be easily generalize to investigate the migration of mesenchymal cells (e.g., invasive MDA-MB-231 breast cancer cells) in 3D ECM. The key modification is to explicitly model ECM degradation by the cells, which can be achieved using the following rule: A migrating cell degrades collagen fibers with a probability $p_b \propto \exp(-r)$, with r being the distance from the fiber to the cell membrane. A degraded fiber is removed from the network in subsequent simulation steps. In addition, cell-cell adhesion can also be easily incorporated into the model to investigate a wide range of cell lines with different phenotypes. With proper modifications and generalizations, as well as efficient parallel implementations, it is expected that the model could be employed to investigate collective migratory behaviors and emergent self-organizing multicellular patterns resulted from ECM-mediated mechanical signaling among the cells.

ACKNOWLEDGMENTS

The authors are extremely grateful to the anonymous reviewers. Y.Z., H.N., and Y.J. thank Arizona State University for the generous startup funds and the University Graduate Fellowships. This work is partially supported by the National Science Foundation Grant No. CMMI-1916878. Q.F., X.W., and F.Y. thank the Chinese Academy of Sciences (CAS), the Key Research Program of Frontier Sciences of CAS (Grant No. QYZDB-SSW-SYS003). L.L. and R.L. thank the National Natural Science Foundation of China (Grants No. 11674043 and No. 11604030). B.S. thanks the Scialog Program for support sponsored jointly by Research Corporation for Science Advancement and the Gordon and Betty Moore Foundation. B.S. is partially supported by the Medical Research Foundation of Oregon and SciRIS-II award from Oregon State University and by the National Science Foundation Grant No. PHY-1400968.

[1] A. J. Ridley, M. A. Schwartz, K. Burridge, R. A. Firtel, M. H. Ginsberg, G. Borisy, J. T. Parsons, and A. R. Horwitz, Cell migration: Integrating signals from front to back, Science **302**, 1704 (2003).

[2] P. Friedl and E.-B. Brocker, The biology of cell locomotion within three-dimensional extracellular matrix, Cell. Mol. Life Sci. CMLS **57**, 41 (2000).

[3] A. Aman and T. Piotrowski, Cell migration during morphogenesis, Dev. Biol. **341**, 20 (2010)

[4] P. Friedl and D. Gilmour, Collective cell migration in morphogenesis, regeneration and cancer, Nat. Rev. Mol. Cell Biol. **10**, 445 (2009).

[5] A. Vaezi, C. Bauer, V. Vasioukhin, and E. Fuchs, Actin cable dynamics and Rho/Rock orchestrate a polarized cytoskeletal architecture in the early steps of assembling a stratified epithelium, Dev. Cell **3**, 367 (2002).

[6] S. Werner, T. Krieg, and H. Smola, Keratinocytefibroblast interactions in wound healing, J. Invest. Dermatol. **127**, 998 (2007).

[7] H. Szurmant and G. W. Ordal, Diversity in chemotaxis mechanisms among the bacteria and archaea, Microbiol. Mol. Biol. **68**, 301 (2004).

[8] S. V. Plotnikov, A. M. Pasapera, B. Sabass, and C. M. Waterman, Force fluctuations within focal adhesions mediate ECM-rigidity sensing to guide directed cell migration, Cell **151**, 1513 (2012).

[9] R. Sunyer, V. Conte, J. Escribano, A. Elosegui-Artola, A. Labernadie, L. Valon, D. Navajas, J. M. García-Aznar, J. J. Munoz, and P. Roca-Cusachs, Collective cell durotaxis emerges from long-range intercellular force transmission, Science **353**, 1157 (2016).

[10] E. Hadjipanayi, V. Mudera, and R. A. Brown, Guiding cell migration in 3D: A collagen matrix with graded directional stiffness, Cell Motil. Cytoskeleton **66**, 121 (2009).

[11] S. B. Carter, Haptotaxis and the mechanism of cell motility, Nature **213**, 256 (1967).

[12] P. P. Provenzano, D. R. Inman, K. W. Eliceiri, S. M. Trier, and P. J. Keely, Contact guidance mediated three-dimensional cell migration is regulated by Rho/ROCK-dependent matrix reorganization, Biophys. J. **95**, 5374 (2008).

[13] J. H. Wang and E. S. Grood, The strain magnitude and contact guidance determine orientation response of fibroblasts to cyclic substrate strains, Connect. Tissue Res. **41**, 29 (2000).

[14] S. Guido and R. T. Tranquillo, A methodology for the systematic and quantitative study of cell contact guidance in oriented collagen gels: Correlation of fibroblast orientation and gel birefringence, J. Cell Sci. **105**, 317 (1993).

[15] R. Ananthakrishnan and A. Ehrlicher, The forces behind cell movement, Int. J. Biol. Sci. **3**, 303 (2007).

[16] M. J. Footer, J. W. J. Kerssemakers, J. A. Theriot, and M. Dogterom, Direct measurement of force generation by actin filament polymerization using an optical trap, Proc. Natl. Acad. Sci. USA **104**, 2181 (2007).

[17] S. Wang and P. G. Wolynes, Active contractility in actomyosin networks, Proc. Natl. Acad. Sci. USA **109**, 6446 (2012).

[18] T. Lecuit, P.-F. Lenne, and E. Munro, Force generation, transmission, and integration during cell and tissue morphogenesis, Annu. Rev. Cell Dev. Biol. **27**, 157 (2011).

[19] M. A. Schwartz, Integrins and extracellular matrix in mechanotransduction, Cold Spring Harbor Perspect. Biol. **2**, a005066 (2010).

[20] G. Totsukawa, Y. Wu, Y. Sasaki, D. J. Hartshorne, Y. Yamakita, S. Yamashiro, and F. Matsumura, Distinct roles of MLCK and ROCK in the regulation of membrane protrusions and focal adhesion dynamics during cell migration of fibroblasts, J. Cell Biol. **164**, 427 (2004).

[21] C. A. Jones, M. Cibula, J. Feng, E. A. Krnacik, D. H. McIntyre, H. Levine, and B. Sun, Micromechanics of cellularized biopolymer networks, Proc. Natl. Acad. Sci. USA **112**, E5117 (2015).

[22] S. B. Lindstrom, D. A. Vader, A. Kulachenko, and D. A. Weitz, Biopolymer network geometries: Characterization, regeneration, and elastic properties, Phys. Rev. E **82**, 051905 (2010).

[23] H. Mohammadi, P. D. Arora, C. A. Simmons, P. A. Janmey, and C. A. McCulloch, Inelastic behavior of collagen networks in cellmatrix interactions and mechanosensation, J. R. Soc. Interface **12**, 20141074 (2015).

[24] S. Nam, K. H. Hu, M. J. Butte, and O. Chaudhuri, Strain-enhanced stress relaxation impacts nonlinear elasticity in collagen gels, Proc. Natl. Acad. Sci. USA **113**, 5492 (2016).

[25] S. Nam, J. Lee, D. G. Brownfield, and O. Chaudhuri, Viscoplasticity enables mechanical remodeling of matrix by cells, Biophys. J. **111**, 2296 (2016).

[26] J. Kim, J. Feng, C. A. Jones, X. Mao, L. M. Sander, H. Levine, and B. Sun, Stress-induced plasticity of dynamic collagen networks, Nat. Commun. **8**, 842 (2017).

[27] S. Chen, W. Xu, J. Kim, H. Nan, Y. Zheng, B. Sun, and Y. Jiao, Novel inverse finite-element formulation for reconstruction of relative local stiffness in heterogeneous extra-cellular matrix and traction forces on active cells, Phys. Biol. **16**, 036002 (2019).

[28] A. D. Doyle, N. Carvajal, A. Jin, K. Matsumoto, and K. M. Yamada, Local 3D matrix microenvironment regulates cell migration through spatiotemporal dynamics of contractility-dependent adhesions, Nat. Commun. **6**, 8720 (2015).

[29] F. Grinnell and W. M. Petroll, Cell motility and mechanics in three-dimensional collagen matrices, Annu. Rev. Cell Dev. Biol. **26**, 335 (2010).

[30] Y. L. Han, P. Ronceray, G. Xu, A. Malandrino, R. D. Kamm, M. Lenz, C. P. Broedersz, and M. Guo, Cell contraction induces long-ranged stress stiffening in the extracellular matrix, Proc. Natl. Acad. Sci. USA **115**, 4075 (2018).

[31] X. Ma, M. E. Schickel, M. D. Stevenson, A. L. Sarang-Sieminski, K. J. Gooch, S. N. Ghadiali, and R. T. Hart, Fibers in the extracellular matrix enable long-range stress transmission between cells, Biophys. J. **104**, 1410 (2013).

[32] P. Ronceray, C. P. Broedersz, and M. Lenz, Fiber networks amplify active stress, Proc. Natl. Acad. Sci. USA **113**, 2827 (2016).

[33] H. Wang, A. Abhilash, C. S. Chen, R. G. Wells, and V. B. Shenoy, Long-range force transmission in fibrous matrices enabled by tension-driven alignment of fibers, Biophys. J. **107**, 2592 (2014).

[34] F. Beroz, L. M. Jawerth, S. Munster, D. A. Weitz, C. P. Broedersz, and N. S. Wingreen, Physical limits to biomechanical sensing in disordered fibre networks, Nat. Commun. **8**, 16096 (2017).

[35] L. Liang, C. Jones, S. Chen, B. Sun, and Y. Jiao, Heterogeneous force network in 3D cellularized collagen networks, Phys. Biol. **13**, 066001 (2016).

[36] H. Nan, Y. Zheng, Y. H. Lin, S. Chen, C. Z. Eddy, J. Tian, W. Xu, B. Sun, and Y. Jiao, Absorbing-active transition in multicellular system regulated by dynamic force network, Soft Matter **15**, 6938 (2019).

[37] A. A. Alobaidi, Y. Xu, Y. Jiao, and B. Sun, Probing cooperative force generation in collective cancer invasion, Phys. Biol. **14**, 045005 (2017).

[38] M. H. Zaman, R. D. Kamm, P. Matsudaria, and D. A. Lauffenburger, Computational model for cell migration in three-dimensional matrices, Biophys. J. **89**, 1389 (2005).

[39] A. Vaziri and A. Gopinath, Cell and biomolecular mechanics in silico, Nat. Mater. **7**, 15 (2008).

[40] P. Masuzzo, M. Van Troys, C. Ampe, and L. Martens, Taking aim at moving targets in computational cell migration, Trends Cell Biol. **26**, 88 (2016).

[41] F. Ziebert, S. Swaminathan, and I. S. Aranson, Modeling for self-polarization and motility of keratocyte fragments, J. R. Soc. Interface **9**, 1084 (2011).

[42] D. Shao, W.-J. Rappel, and H. Levine, Computational Model for Cell Morphodynamics, Phys. Rev. Lett. **105**, 108104 (2010).

[43] D. Shao, H. Levine, and W. J. Rappel, Coupling actin flow, adhesion, and morphology in a computational cell motility model, Proc. Natl. Acad. Sci. USA **109**, 6851 (2012).

[44] U. Z. George, A. Stephanou, and A. Madzvamuse, Mathematical modeling and numerical simulations of actin dynamics in the eukaryotic cell, J. Math. Biol. **66**, 547 (2013).

[45] T. C. Bidone, W. Jung, D. Maruri, C. Borau, R. D. Kamm, and T. Kim, Morphological transformation and force generation of active cytoskeletal networks, PLoS Comput. Biol. **13**, e1005277 (2017).

[46] M. C. Kim, J. Whisler, Y. R. Silberberg *et al.*, Cell invasion dynamics into a three dimensional extracellular matrix fibre network, PLoS Comput. Biol. **11**, e1004535 (2015).

[47] T. Vicsek, A. Czirok, E. Ben-Jacob, I. Cohen, and O. Shochet, Novel Type of Phase Transition in a System of Self-Driven Particles, Phys. Rev. Lett. **75**, 1226 (1995).

[48] C. Bechinger, R. Di Leonardo, H. Lowen, C. Reichhardt, G. Volpe, and G. Volpe, Active particles in complex and crowded environments, Rev. Mod. Phys. **88**, 045006 (2016).

[49] D. Bi, J. Lopez, J. Schwarz, and M. L. Manning, A density-independent rigidity transition in biological tissues, Nat. Phys. **11**, 1074 (2015).

[50] F. Graner and J. A. Glazier, Simulation of Biological Cell Sorting Using a Two-Dimensional Extended Potts Model, Phys. Rev. Lett. **69**, 2013 (1992).

[51] Y. Jiao and S. Torquato, Emergent properties from a cellular automaton model for invasive tumor growth in heterogeneous environment, PLoS Comput. Biol. **7**, e1002314 (2011).

[52] Y. Jiao and S. Torquato, Diversity of dynamics and morphologies of invasive solid tumors, AIP Adv. **2**, 011003 (2012).

[53] Y. Jiao and S. Torquato, Evolution and morphology of microenvironment-enhanced malignancy of three-dimensional invasive solid tumors, Phys. Rev. E **87**, 052707 (2013)

[54] H. Xie, Y. Jiao, Q. Fan *et al.*, Modeling three-dimensional invasive solid tumor growth in heterogeneous microenvironment under chemotherapy, PLoS ONE **13**, e0206292 (2018).

[55] J. Lober, F. Ziebert, and I. S. Aranson, Modeling crawling cell movement on soft engineered substrates, Soft Matter **10**, 1365 (2014).

[56] J. Lober, F. Ziebert, and I. S. Aranson, Collisions of deformable cells lead to collective migration, Sci Rep. **5**, 9172 (2015).

[57] A. Goychuk, D. B. Brückner, A. W. Holle, J. P. Spatz, C. P. Broedersz, and E. Frey, Morphology and motility of cells on soft substrates, arXiv:1808.00314.

[58] H. Abdel-Rahman, B. Thomas, and T. Kim, A mechanical model for durotactic cell migration, ACS Biomater. Sci. Eng. **5**, 3954 (2019).

[59] M. Dietrich, H. Le Roy, D. B. Bruckner, H. Engelke, R. Zantl, J. O. Radler, and C. P. Broedersz, Guiding 3D cell migration in deformed synthetic hydrogel microstructures, Soft Matter **14**, 2816 (2018).

[60] M. F. Staddon, D. Bi, A. P. Tabatabai, V. Ajeti, M. P. Murrell, S. Banerjee *et al.*, Cooperation of dual modes of cell motility promotes epithelial stress relaxation to accelerate wound healing, PLoS Comput. Biol. **14**, e1006502 (2018).

[61] V. Ajeti, A. P. Tabatabai, A. J. Fleszar, M. F. Staddon, D. S. Seara, C. Suarez, M. S. Yousafzai, D. Bi, D. R. Kovar, S. Banerjee, and M. P. Murrell, Wound healing coordinates actin architectures to regulate mechanical work, Nat. Phys. **15**, 696 (2019).

[62] E. N. Schaumanna, M. F. Staddon, M. L. Gardel, and S. Banerjee, Force localization modes in dynamic epithelial colonies, Mol. Biol. Cell **29**, 2835 (2018).

[63] J. Feng, H. Levine, X. Mao *et al.*, Stiffness sensing and cell motility: Durotaxis and contact guidance, Soft Matter **15**, 4856 (2019).

[64] J. Zhu and A. Mogilner, Comparison of cell migration mechanical strategies in three-dimensional matrices: A computational study, Interface Focus **6**, 20160040 (2016).

[65] A. Moure and H. Gomez, Phase-field model of cellular migration: Three-dimensional simulations in fibrous networks, Comput. Methods Appl. Mech. Eng. **320**, 162 (2017).

[66] A. Moure and H. Gomez, Three-dimensional simulation of obstacle-mediated chemotaxis, Biomech. Model. Mechanobiol. **17**, 1243 (2018).

[67] H. Nan, L. Liang, G. Chen, L. Liu, R. Liu, and Y. Jiao, Realizations of highly heterogeneous collagen networks via stochastic reconstruction for micromechanical analysis of tumor cell invasion, Phys. Rev. E **97**, 033311 (2018).

[68] C. Jones, L. Liang, D. Lin, Y. Jiao, and B. Sun, The spatial-temporal characteristics of type I collagen-based extracellular matrix, Soft Matter **10**, 8855 (2014).

[69] S. Kirkpatrick, C. D. Gelatt Jr., and M. P. Vecchi, Optimization by simulated annealing, Science **220**, 671 (1983).

[70] D. A. Head, A. J. Levine, and F. C. MacKintosh, Mechanical response of semiflexible networks to localized perturbations, Phys. Rev. E **72**, 061914 (2005).

[71] Y. Shokef and S. A. Safran, Scaling Laws for the Response of Nonlinear Elastic Media With Implications for Cell Mechanics, Phys. Rev. Lett. **108**, 178103 (2012).

[72] J. Steinwachs, C. Metzner, K. Skodzek *et al.*, Three-dimensional force microscopy of cells in biopolymer networks, Nat. Method **13**, 171 (2016).

[73] C. Heussinger and E. Frey, Force distributions and force chains in random stiff fiber networks, Eur. Phys. J. E **24**, 47 (2007).

[74] B. Burkel, M. Proestaki, S. Tyznik, and J. Notbohm, Heterogeneity and nonaffinity of cell-induced matrix displacements, Phys. Rev. E **98**, 052410 (2018).

[75] S. Tyznik and J. Notbohm, Length scale dependent elasticity in random three-dimensional fiber networks, Mech. Mater. **138**, 103155 (2019).

[76] S. K. Boey, D. H. Boal, and D. Discher, Simulations of the erythrocyte cytoskeleton at large deformation. I. Microscopic models, Biophys. J. **75**, 1573 (1998).

[77] D. Discher, D. H. Boal, and S. K. Boey, Simulations of the erythrocyte cytoskeleton at large deformation. II. Micropipette aspiration, Biophys. J. **75**, 1584 (1998).

[78] M. F. Coughlin and D. Stamenovic, A prestressed cable network model for the adherent cell cytoskeleton, Biophys. J. **84**, 1328 (2003).

[79] D. Gordon, A. Bernheim-Groswasser, C. Keasar, and O. Farago, Hierarchical self-organization of cytoskeletal active networks, Phys. Biol. **9**, 026005 (2012).

[80] Q. Fan, Y. Zheng, H. Nan, Y. Jiao, and F. Ye (unpublished).